Environmental Science Advances

ROYAL SOCIETY OF CHEMISTRY

PAPER

View Article Online
View Journal | View Issue

Cite this: *Environ. Sci.: Adv.*, 2024, **3**, 1775

WO_3/Pt photocatalyst supported by a ceramic filter for indoor air purification under visible light irradiation†

Sudipto Pal, *[a] Amruth Kaitheri,[a] Sanosh Kunjalukkal Padmanabhan,[a] Massimo Catalano,[bc] Stefano Perboni[d] and Antonio Licciulli[a]

Received 6th June 2024
Accepted 8th October 2024

DOI: 10.1039/d4va00188e

rsc.li/esadvances

Household air pollution exposure can lead to various diseases, including stroke, ischaemic heart disease, chronic obstructive pulmonary disease (COPD), and lung cancer. In this study, an indoor air purification technique was developed employing a visible light-activated photocatalyst consisting of a WO_3/Pt-coated ceramic foam filter (CFF). Under visible light irradiation, the coated porous filter was able to decompose toluene, a prevalent indoor air contaminant. The interconnected three-dimensional structure of the CFF with open pores facilitated toluene adsorption and simultaneous decomposition by the photocatalyst. XRD analysis revealed that WO_3/Pt had tungsten oxide in a monoclinic crystal structure with immiscible platinum metal clusters. The specific surface area and pore diameter were analyzed using the BET method, while the energy band gap was determined using DRS. XRF spectroscopy was used to find the percentage composition of the material, and structural and morphological studies of the samples were conducted using TEM and FESEM analyses. Photodegradation studies were performed for toluene removal, demonstrating a significant drop in toluene concentration in a short period (99.1% degradation in 150 min). A comparative investigation of the visible light photoactivity of WO_3/Pt and TiO_2 (P25) in water was conducted utilizing dye degradation tests, and WO_3/Pt dominated with its excellent degradation efficiency.

Environmental significance

Indoor air pollution due to the emission of several volatile organic compounds (VOCs) from household products or processes can lead to serious health issues, including chronic respiratory diseases. Poor ventilation systems in more energy-efficient buildings can mean people are exposed to VOCs for prolonged periods of time. Moreover, the extensive use of popular air purification devices equipped with UV lights can trigger the unwanted release of VOCs beyond the permitted level. To address this issue, we propose an air-cleaning system, where VOCs can be decomposed efficiently by an advanced oxidation process using visible light as the source of radiation. We demonstrate a WO_3/Pt nanocluster-coated porous ceramic filter that is highly effective at eliminating gaseous toluene and that could allow cleaning the indoor airspace for a healthier indoor environment. The coated ceramic filter could be installed in an air cleaning device that can be used in the long run and reused by simple washing, without the necessity to replace it periodically, thus contributing towards a greener environment.

1 Introduction

Volatile organic compounds (VOCs) are hazardous organic molecules with low water solubility and high vapor pressure at room temperature with boiling points between 50 and 260 °C at atmospheric pressure.[1,2] VOCs are emitted in the form of gases from many household products as well as from modern building materials and can eventually react with other gaseous molecules to form a wide range of harmful pollutants, especially in the indoor airspace. Long-term exposure to VOCs in the indoor atmosphere may contribute to chronic and acute health conditions, which are often termed as sick building syndrome.[3] Although VOCs are present in both indoor and outdoor environments, the concentration indoors can be much higher than that outdoors due to a lack of sufficient ventilation and the presence of off-gassing materials inside some buildings.[4] Among the various VOCs, acetaldehyde, formaldehyde, benzene and toluene are most common due to their presence in certain domestic products, like cleaning materials, disinfectants, cosmetics and deodorants, arts and crafts materials (paint, glue, permanent markers, *etc.*); building and furnishing

[a]*Department of Engineering for Innovation, University of Salento, Campus Ecotekne, Via per Monteroni, 73100 Lecce, Italy. E-mail: sudipto.pal@unisalento.it*

[b]*Department of Mathematics and Physics "Ennio De Giorgi", University of Salento, Via Arnesano, 73100 Lecce, Italy*

[c]*Institute for Microelectronics and Microsystems (IMM), CNR, Via Monteroni, 73100 Lecce, Italy*

[d]*Nanohub Srl, Via Borgonuovo 9, 20121 Milano, Italy*

† Electronic supplementary information (ESI) available. See DOI: https://doi.org/10.1039/d4va00188e

materials, like paints and varnishes, sealants, adhesives, and flooring; and office equipment, like printers and copiers.[1,5,6] Therefore, it is important to develop an efficient way to remove VOCs from indoor airspaces.

There are several strategies for the elimination of VOCs and airborne toxins, the most common being adsorption, in which porous and high surface area materials, like activated carbon, biochar, and zeolites, are used as adsorbents in filters media.[7–9] The most commonly found adsorbent filter in air-purifying devices is the high-efficiency particulate air (HEPA) filter, which can capture particles as small as 0.3 microns, such as dust, pollen, pet dander, and smoke. However, its saturated adsorption capability, pore blockage, and condensation limit its applicability since these filters require regular maintenance and eventually complete replacement after a certain time period, leading to additional waste disposal issues.[1,3,10] Chemical and catalytic oxidation processes are also promising solutions, due to their higher efficiency, but each has its own limitations in indoor conditions. For instance, the performance of chemical processes can be very selective and produce secondary by-products, whereas catalytic processes require a higher operating temperature to completely decompose VOCs, which makes their practical use unfeasible.[1] In contrast, photocatalytic oxidation (PCO) is a promising and relatively safe technology for air purification, wherein UV/visible light and catalysts are used to break down and neutralize VOCs and airborne pathogens.[10,11] To date, TiO_2 has been one of the most explored photocatalysts in water and air purification because of its many advantageous properties, like low cost, easy availability, photostability, and non-toxicity.[12–15] However, due to its high band gap energy (E_g = 3.2 eV), TiO_2 is only active in UV light and so most commercial air-cleaning devices use combinations of light sources, where either a germicidal UV lamp (emission at 222 nm) or traditional 254 nm mercury UV lamp is equipped as the odour-killing light source.[16,17] In the last few years, due to the COVID-19 pandemic, there has been a surge in interest in these devices to combat airborne pollutants. However, recent studies have found that these devices can readily produce ozone (O_3) as a by-product, which can then react with other gaseous pollutants and re-contaminate the airspace by creating harmful aerosol species, which raises safety concerns of using them in indoor airspaces.[6,16–18] Continuous ventilation and a fresh air flow are thus required to avoid secondary air contamination, which would not be an economical solution for frequent use in many buildings. In this regard, applying PCO under visible light irradiation could be a safer yet still efficient way to decompose VOCs and improve the indoor air quality.[19,20] Among several visible light-active photocatalysts, tungsten oxide (WO_3) in its nanostructured phase is highly promising due to its many advantageous properties, like narrow energy band gap (2.4–2.8 eV), non-toxicity, earth abundance, physico-chemical and thermal stability, relatively low cost, and the high oxidation power of its valence band (VB) holes (+3.1–3.2 V_{NHE} at pH 0).[21–23] Owing to the higher valence band position compared to the oxidation potential of water (E_{H_2O/O_2} + 1.23 V_{NHE}), it can produce $^{\bullet}OH$ radicals through photogenerated holes, which can facilitate photocatalytic degradation of organic pollutants in aqueous media.[22,24,25] However, due to the lower position of the conduction band (CB) edge of WO_3 (+0.3–0.5 V_{NHE}), it cannot provide sufficient potential for single-electron reduction of the adsorbed O_2 to produce superoxide anion radicals (reduction potential of $O_2/O_2^{\bullet-}$ = −0.28 V_{NHE}; $O_2/HO_2^{\bullet}$ = −0.046 V_{NHE}).[25,26] This leads to a fast recombination of the photogenerated CB electrons and VB holes on the surface of WO_3, resulting in the poor photocatalytic activity of WO_3, particularly to decompose gaseous species in the air.[25,26] To overcome this problem, the most popular way is to modify WO_3 by intimately mixing it with different co-catalysts (mainly Au, Ag/Ag_2O, Cu/Cu_2O, Pt, Pd, Ru, Fe_2O_3, MnO_2, V_2O_5, and carbon dots).[27–31] In particular, several studies have indicated that a small amount of Pt addition to the WO_3 photocatalyst can enormously increase its efficiency, whereby Pt act as the sink for the photogenerated electrons, which can accelerates O_2 reduction *via* a multielectron reduction process.

In the present study, we focused on the photocatalytic decomposition of gaseous toluene using a WO_3/Pt-coated ceramic foam filter as a cost-effective, energy-efficient, and environment friendly substrate for indoor air-filtration systems. Additionally, the efficiency of WO_3/Pt as a visible light-active photocatalyst for wastewater treatment was also investigated. Compared to conventional filters, like HEPA, ceramic foam filters (CFFs) are a more favourable and sustainable solution for many filtration applications since they are robust, thermodynamically stable, recyclable, and eco-friendly.[10,32,33] After multiple filtration cycles, the particulate depositions can be easily washed away under a water flow and eventually the CFFs can be regenerated manifold times by thermal treatment since they possess high thermal and mechanical shock resistance.[10,34,35] Nevertheless having a compact though porous structure means it can treat polluted air without occupying much space in a purifying device while maintaining minimal pressure drop. Furthermore, owing to its high porosity, hydrophilic surface, and chemical/mechanical resistance, it can be easily coated with any aqueous photocatalyst suspension by dipping, spraying, or a simple immersion technique. To the best of our knowledge, there is no such report where WO_3/Pt-coated ceramic foam filters have been used as a visible light (λ > 420 nm)-active supported catalyst in indoor air purification.

2 Experimental section

2.1. Supported catalyst preparation

Visible light-active platinum (Pt)-doped tungsten trioxide (WO_3), herein denoted as WO_3/Pt (LG Hausys PLATROM), was used as the photocatalyst material in the experiments. Aeroxide P25 titanium dioxide (TiO_2) (Evonik Corporation, Hanau, Germany; average particle size 25 nm, BET surface area ~ 50 m^2 g^{-1}, 80% anatase and 20% rutile) was used as the reference photocatalyst. An aluminosilicate (Al_2O_3 ~ 86.43 wt%, SiO_2 ~ 13.10 wt%) ceramic foam filter (VUKOPOR® A, LANIK s.r.o., Boskovice, Czech Republic) with a three-dimensional (3D) and interconnected network of opened pores (10 pores per inch) was used as the catalyst support. WO_3/Pt nanoclusters were uniformly deposited on the ceramic filter surface by the

immersion technique from an aqueous suspension of WO_3/Pt nanometric powder. A homogeneous suspension of WO_3/Pt in H_2O (8% w/v) was prepared by mixing the required amount of the powder in deionized water with simultaneous mechanical stirring and ultrasonication for 30 min. The coating deposition was achieved by immersing and withdrawing the filters in the suspension followed by oven drying at 80 °C overnight. The amount of photocatalyst loading was controlled by varying the number of immersions in the suspension. In our case, the trade-off between maintaining open pores and the photocatalyst loading was optimized by applying only one immersion. Pure WO_3 was prepared by annealing the required amount of ammonium metatungstate hydrate ($(NH_4)_6H_2W_{12}O_{40}\cdot xH_2O$, ≥85% WO_3 basis, Merck KGaA, Germany) in a muffle furnace at 550 °C for 2 h in the air atmosphere.

2.2. Catalyst and support characterization

The crystalline structure of WO_3/Pt was analyzed by X-ray diffraction (XRD) using a Rigaku Ultima diffractometer with Cu Kα ($\lambda = 1.5406$ Å) radiation operated at 40 kV and 20 mA with a scanning step of 0.02°. The specific surface area of the photocatalyst powder was measured from the N_2 adsorption–desorption isotherms using the Brunauer–Emmett–Teller (BET) method plot with an Anton-Parr NOVA 2200e surface area and pore size analyzer. The optical characteristics of the photocatalyst powders were determined from the UV-visible absorption spectra measured in the diffuse reflectance spectroscopy (DRS) mode using an Agilent Cary 5000 UV-visible-NIR spectrophotometer fitted with a 110 mm diameter polytetrafluoroethylene (PTFE)-coated integrating sphere. The chemical compositions of the samples were analyzed with a Bruker M4 Tornado micro X-ray fluorescence spectrometer (μ-XRF) operated at 30 kW (50 kV, 600 μA). To get the optimum results, the X-ray power source was fixed at 50 kV, 480 μA, and the spectra were recorded under 20 mbar vacuum. Elemental quantification was performed with the inbuilt M-Quant software. Morphological characterization of the WO_3/Pt nanoparticles was performed by transmission electron microscopy (TEM) measurements with a 200 kV JEOL electron microscope. High-resolution TEM (HRTEM) analyses and selected area electron diffraction (SAED) patterns were recorded to identify the different phases of the WO_3 and Pt nanocrystals. To perform the TEM measurements, the photocatalyst powder (0.1 g) was dispersed in 1 mL ethanol under sonication and a drop of the suspension was cast on a carbon-coated copper grid. The morphology and microstructural properties of the photocatalyst powder as well as those of bare and WO_3/Pt-coated ceramic foam filters were examined with an EVO-Zeiss (Jena, Germany) field emission scanning electron microscopy (FESEM) system.

2.3. Photocatalytic performance for waste water treatment

The photocatalytic activities of the WO_3/Pt and P25 TiO_2 powders in waste water treatment were evaluated by observing the degradation of Rhodamine B (RhB) and Methylene Blue (MB) dye molecules in aqueous medium inside a custom-built

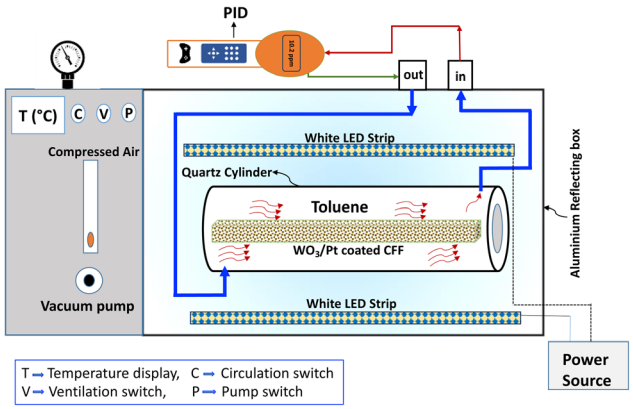

Fig. 1 Schematic diagram of the photocatalytic reactor showing the experimental set-up for toluene photodegradation.

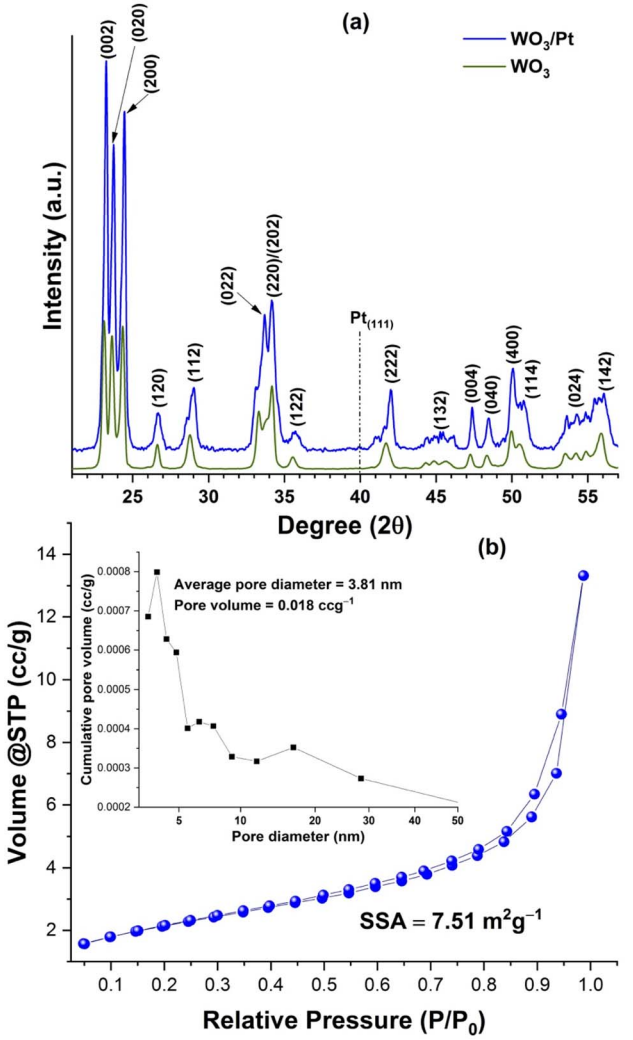

Fig. 2 (a) XRD pattern of the WO_3/Pt nanocomposite and pure WO_3 powder; the corresponding *hkl* planes of the respective diffraction peaks are indexed in the graph. (b) N_2 adsorption–desorption isotherm and pore-size distribution (inset) of the WO_3/Pt nanocomposite.

photoreactor consisting of a solar lamp, magnetic stirrer, and cooling system. A 300 W tungsten lamp (spectral radiation distribution: 280–315 nm ~ 1.8 W m^{-2}, 315–400 nm ~ 11.0 W m^{-2}, and 380–780 nm ~ 39.0 W m^{-2}) was used as the natural source of sunlight. A commercial UV cut-off filter ($\lambda \leq 315$ nm) was used to investigate the effect of UVB/UVC light irradiation on the photocatalytic efficiency. In a typical experiment, the required amount of catalyst (1 g L^{-1}) was dispersed in 5 ppm of 200 mL aqueous dye solution (both RhB and MB) and kept stirring inside the reactor in the dark to achieve adsorption–desorption equilibrium. After that, the solution was subjected to solar-light irradiation and an aliquot was taken at certain time intervals for the spectrophotometric studies. Each sample was centrifuged at 12 000 rpm before the spectrophotometric measurements. The photocatalytic degradation rates of RhB and MB were monitored by measuring the intensity of the dyes' absorption maxima at 554 and 650 nm, respectively.

2.4. Toluene photodegradation evaluation

The photocatalytic degradation tests of toluene in visible light were performed in a cylindrical quartz reactor (effective volume 3 L) at atmospheric pressure. Two white LED strips (40 W, 31.6 W m^{-2}, $\lambda \geq 420$ nm) were used as the visible light source to replicate the indoor lighting condition. Before using the ceramic foam filter, the catalyst powders (WO_3/Pt, pure WO_3, and P25 TiO_2) were tested to verify the efficiency of the unsupported catalysts in visible light. Typically, 3 g of catalyst powder were spread on a flat glass and placed inside the reactor. After that, 2 μL of toluene was injected inside the closed reactor and the air containing toluene vapor was recirculated in a closed loop with a pump. A pictorial diagram of the photocatalytic reactor is shown in Fig. 1. The concentration of toluene inside the reactor was monitored using a photoionization detector (PID) instrument at a resolution of 0.1 ppm (Tiger, ION Science Ltd). The VOC detector relied on the suction of the gas through the inlet probe and exhausting the gas to the outlet probe after passing through the PID sensor assembly. It was fitted with a 10.6 eV krypton PID lamp, which measured the concentration of ionized gas (toluene ionization energy ~ 8.82 eV, response factor = 0.56 with a 10.6 eV lamp). The working condition of the PID instrument is shown in the schematic diagram in Fig. 1. The measured gas concentration was recorded and displayed on the LCD screen of the instrument in real time. The PID instrument was connected to the quartz reactor in a closed loop to avoid any loss of the gaseous toluene through the exhaust valve of the instrument. After recirculating the toluene (50–60 ppm) for a certain time period in the dark, its concentration inside the reactor became steady due to the

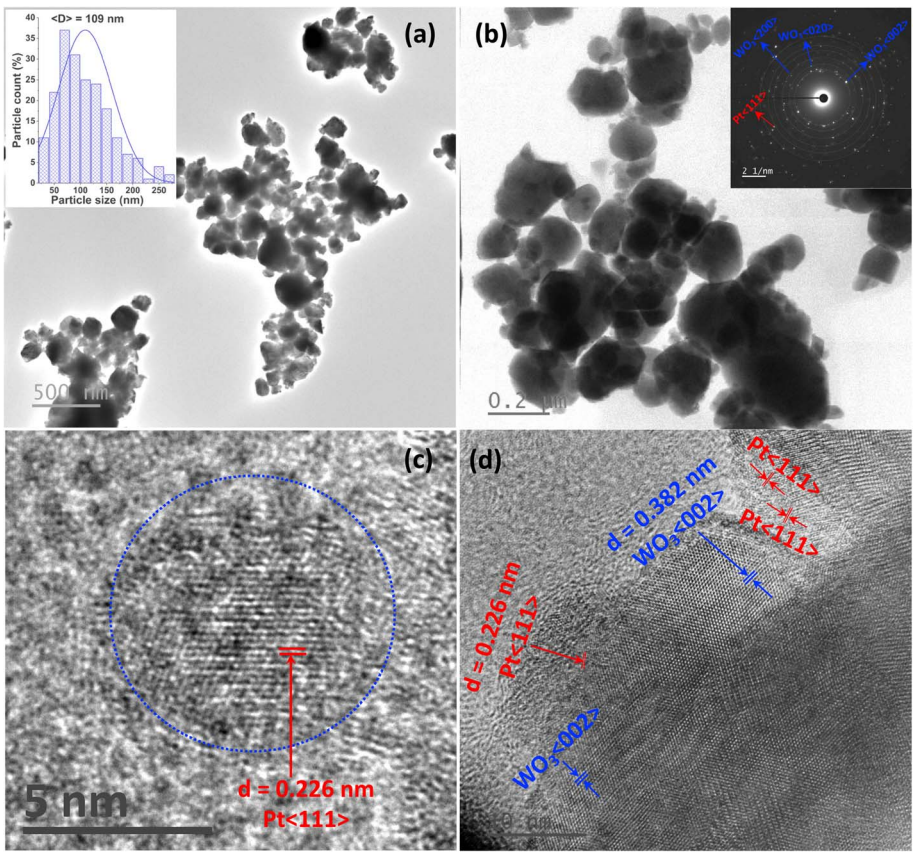

Fig. 3 (a and b) Bright-field TEM images of the WO_3/Pt nanoparticles, along with a histogram of the particle-size distribution (inset of (a)) and the corresponding SAED pattern (inset of (b)). (c and d) HRTEM images at different magnifications: (a and b) low magnification images showing the distribution of the WO_3/Pt nanoparticles.

attainment of adsorption–desorption equilibrium. At this point, the LED lights were switched on and the toluene concentration was recorded together with the visible light exposure time. For both the coated/uncoated filters, the measurements were carried out in similar way by placing the filters inside the reactor.

3 Results and discussions

The XRD patterns of the WO_3/Pt nanocomposite and pure WO_3 are shown in Fig. 2a. Both the pure WO_3 and WO_3/Pt nanocomposite showed similar diffraction peaks. The peaks at 2θ positions of 23.24°, 23.72°, 24.4°, 26.72°, and 28.8° could be assigned to the (002), (020), (200), (120), and (112) reflection planes of the pure monoclinic WO_3 crystal structure (m-WO_3, JCPDS #72-0677).[36,37] The well-defined and intense peaks indicated the highly crystalline monoclinic structure of WO_3 in both cases. Whereas the appearance of a weak peak at $2\theta \sim 39.7°$ in the WO_3/Pt sample indicated the formation of face centred cubic (fcc) Pt in the WO_3/Pt nanostructure. The weak intensity of this peak could be due to the lower amount of Pt present in the WO_3/Pt composite as well as the smaller size of the Pt NPs compared to WO_3.

Fig. 2b shows the N_2 adsorption–desorption isotherm along with the pore-size distribution (shown as the inset) calculated from the desorption isotherm branch using the Barrett–Joyner–Halenda (BJH) method. The volume@STP *vs.* partial pressure curve presented a type (II) adsorption curve, which indicated multilayer adsorption on the surface of the sample at medium pressure followed by capillary condensation at higher pressures, revealing the sample was non-porous.[38] The lower specific surface area (7.51 $m^2\ g^{-1}$) and pore volume (0.018 $cm^3\ g^{-1}$) obtained also suggested this observation.

The shape and size distribution of the WO_3/Pt nanocomposite particles were next explored by TEM analyses and are reported in Fig. 3. The low-resolution bright-field image (Fig. 3a) revealed the near spherical shape of the particles having a size distribution between 25 and 270 nm, with an average diameter of about 109 nm, as seen from the histogram of the particle-size distribution (inset of Fig. 3a). This observation was also reflected in the higher magnification image shown in Fig. 3b. Here two different sets of nanoclusters could be observed: bigger particles with light contrast, which existed mostly in an agglomerated state, and smaller particles with dark contrast, with an uneven distribution. The bigger particles could be identified as WO_3 and the smaller ones (~4–10 nm diameter) as Pt nanoparticles. The selected area electron diffraction (SAED) pattern, which is shown as inset of Fig. 3b, confirmed the presence of both WO_3 and Pt. The high-resolution TEM (HRTEM) micrographs are shown in Fig. 3c and d, where the inter-planar distance (*d* spacings) of the smaller particles was about 0.226 nm, corresponding to the (111) plane of fcc Pt,[39] whereas for the larger particles it was 0.382 nm, confirming the (002) plane of monoclinic WO_3, which was in accord with the XRD analysis.

The visible light absorption of the WO_3/Pt photocatalyst was evaluated through the UV-visible diffuse absorption spectra presented in Fig. 4a. The spectra of pure WO_3 and TiO_2 are shown for comparison. The curves presented are the directly measured absorption spectra of the respective photocatalyst powder samples in the DRS mode. From the absorption curves, it could be observed that the pure WO_3 and TiO_2 exhibited absorption band edges at about 452 nm and 390 nm, respectively, whereas the band edge for WO_3/Pt was at 487 nm, confirming the ability of WO_3/Pt to be excited under visible light irradiation. The extended broad absorption of WO_3/Pt over the entire visible wavelength region (*ca.* 460–800 nm) could be contributed from the surface plasmon resonance (SPR) of the Pt NPs,[39,40] which was absent in pure WO_3. The band gap energies (E_g) of the samples were estimated from the Tauc formula by plotting $(\alpha h\nu)^{1/n}$ against the photon energy ($h\nu$, hence the incoming light wavelength), where 'α' is the optical absorption coefficient and the exponent 'n' is the allowed electronic transition in WO_3 semiconductors.[41] The value of $n = 2$, which represents the indirect allowed transition for WO_3, allowed

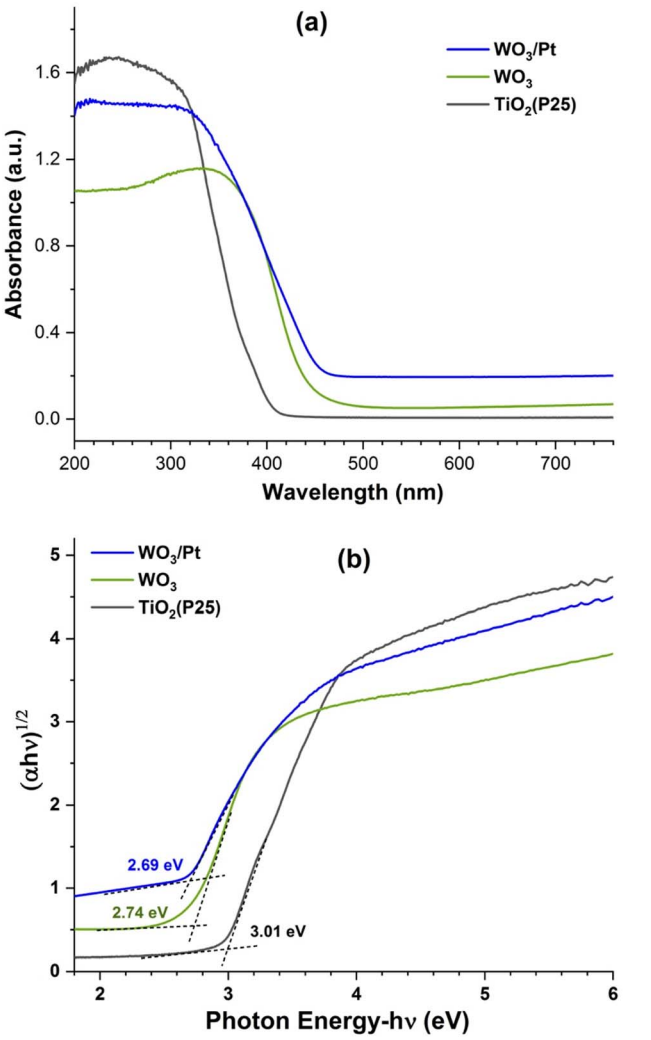

Fig. 4 (a) UV-visible diffuse reflectance spectra in the absorbance scale of the WO_3/Pt nanocomposite powder, pure WO_3 powder, and commercial TiO_2 (P25) powder. (b) Plots of $(Ah\nu)^{1/2}$ against the photon energy $h\nu$ (eV) for the respective samples.

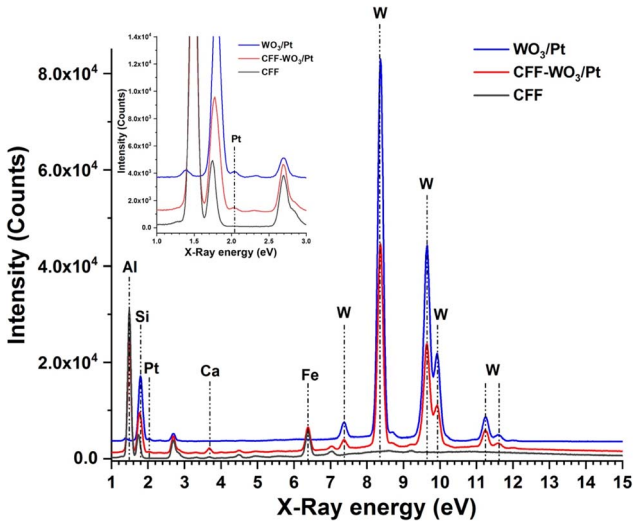

Fig. 5 X-ray fluorescence (XRF) spectra of bare CFF, WO_3/Pt-coated CFF, and WO_3/Pt powder (plotted from bottom to top).

Table 1 Chemical composition of the CFF, WO_3/Pt-coated CFF, and pure WO_3/Pt as quantified from XRF analysis

	Oxides/elements (wt%)						
Samples	Al_2O_3	SiO_2	Fe_2O_3	TiO_2	CaO	WO_3	Pt
CFF	86.43	13.10	0.27	0.12	0.07	—	—
WO_3/Pt-CFF	84.03	12.19	0.24	0.07	0.05	3.28	0.12
WO_3/Pt	—	—	—	—	—	96.25	3.75

direct evaluation of the optical band gap energy, as shown in Fig. 4b. The intersection between the extrapolation of the linear plot and the photon energy gave the estimation of the E_g values as 2.69, 2.74, and 3.01 eV for WO_3/Pt, pure WO_3, and TiO_2, respectively, which were in good agreement with the reported values.[12,41]

Next, X-ray fluorescence (XRF) measurements were performed on the WO_3/Pt nanocomposite and coated/uncoated ceramic filters to obtain the chemical composition and distribution of WO_3/Pt on the filter surface. The XRF spectra measured on WO_3/Pt powder, bare ceramic filter (CFF), and WO_3/Pt-coated CFF are shown in Fig. 5, where the elements are marked according to their energy peak positions. The chemical compositions of the respective samples (in wt%) calculated from the spectral distribution of the elements are also reported in Table 1. The bare filter consisted mainly alumina and silica with a ratio close to the mullite composition, as also disclosed from the technical data sheet provided by the filter manufacturer. The Pt content in the WO_3/Pt nanocomposite was found to be ~3.75 wt% with respect to WO_3, whereas the total loading of WO_3/Pt on the filter was about 3.4 wt%. The inset of Fig. 5 shows an enlarged portion of the spectra in the lower energy region to show the presence of Pt, where a very weak peak was observed compared to that from tungsten, which was in agreement with the presence of a lower amount of Pt in the WO_3/Pt nanostructure. The chemical mapping of the elemental distribution at lower and higher magnifications is reported in Fig. S2,† where a continuous distribution of WO_3 and Pt was observed throughout the branches of the coated filter, confirming their even deposition on the substrate. This was also supported by the appearance of the coated filter with respect to the uncoated one in Fig. S1,† where digital photographs of these filters are presented.

Structural and morphological studies of the uncoated and WO_3/Pt-coated filter were performed using FESEM analysis. The FESEM images with different magnifications of the WO_3/Pt nanoparticles, bare filter, and WO_3/Pt-coated filter are shown in Fig. 6. A closer look at the SEM images of the WO_3/Pt powder (Fig. 6a and b) revealed that the nanoclusters were made up of spherical particles linked to each other, as validated by the TEM analyses (Fig. 3). Fig. 6c and d show the planar and cross-sectional views of the bare ceramic filter's branches, revealing its porous nature with the pores belonging to the macroporous range. The higher magnification image of the cross-section shown in the inset of Fig. 6c gives a clearer view, in which large pores and mullite crystals with grain sizes of 2–5 μm are visible. A hollow channel, which was interconnected through various branches of the 3D structure, could also be noticed that may favour the adsorption of gaseous pollutants. Fig. 6e–h show the images of WO_3/Pt-coated ceramic filters with different magnifications, presenting clear evidence that WO_3/Pt was evenly deposited on the porous surface of the filter material. Although most of the particles were deposited on the outer surface of the filter, some of them reached the inner part as well due to the porous characteristic of the filter, as demonstrated in Fig. 6f–h.

Aside from the VOC photodecomposition measurements, the WO_3/Pt and TiO_2 powder samples were tested to determine their photocatalytic ability by dye degradation experiments under solar-light illumination. The UV-visible spectral evolutions of RhB and MB dyes against the light-irradiation time for the WO_3/Pt and TiO_2 photocatalyst powder samples are shown in Fig. S4.† The photocatalytic reaction rate constants calculated from the plots of C/C_0 (Fig. S5†) against the reaction time under various experimental conditions are reported in Table S1.† It was evidenced that in all the cases, the reaction rate constant of WO_3/Pt was higher than that of TiO_2. We also checked the influence of UVB/UVC wavelength on the photocatalytic performance by adding a 315 nm cut-off filter during solar-light irradiation. It was evident that this had only a little effect on the photocatalytic performance of WO_3/Pt, whereby the efficiency decreased by 10.6% and 5.55% for the RhB and MB dyes; whereas the efficiency of TiO_2 was decreased by 33.33% and 28.57% for RhB and MB, respectively. This data indicated the higher performance of WO_3/Pt in the near-visible wavelength range, which was supported by the optical absorption spectra reported in Fig. 3a.

The photocatalytic decomposition of toluene used as a model for VOC air pollutants was performed with the WO_3/

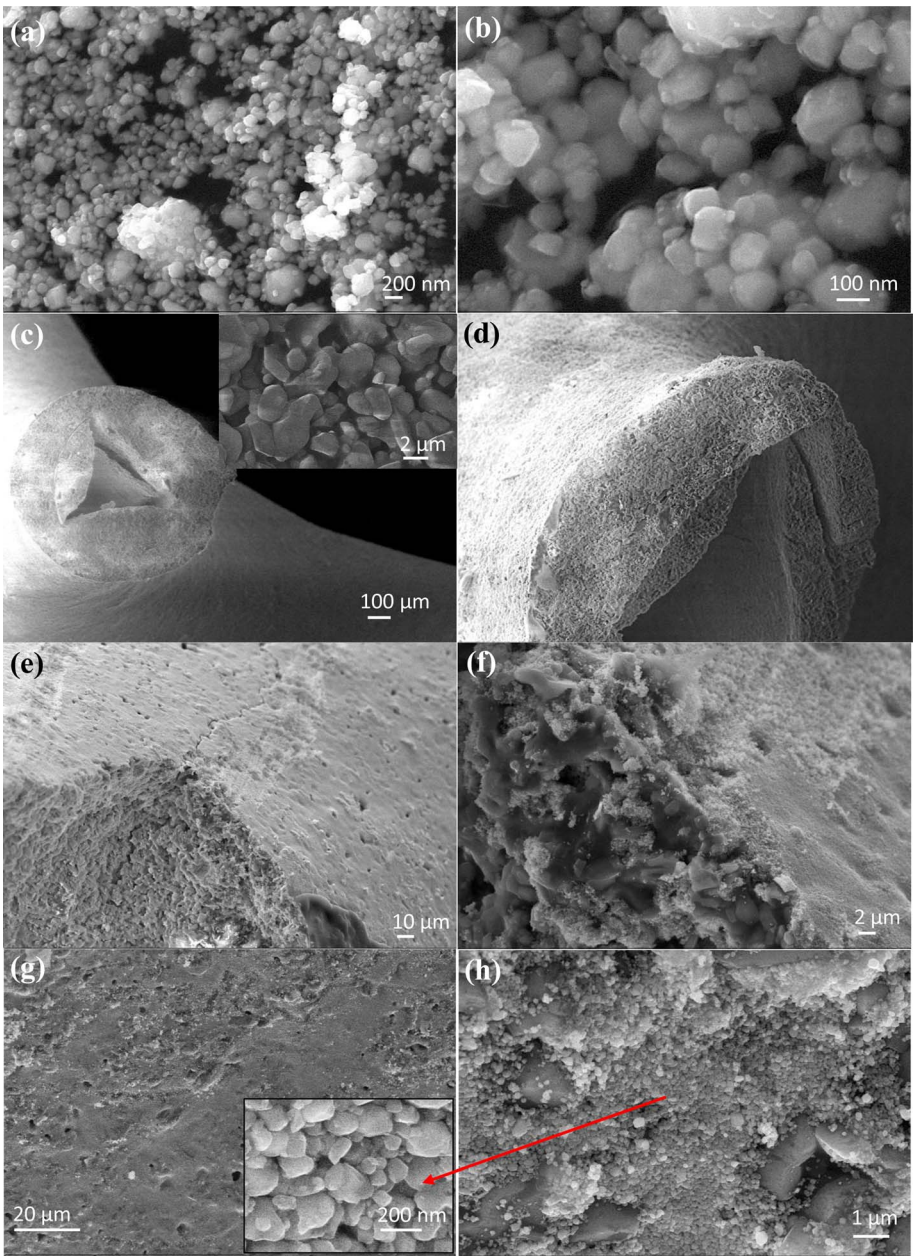

Fig. 6 FESEM images of (a) and (b) WO_3/Pt particles; (c) and (d) bare ceramic filter, and (e–h) WO_3/Pt-coated ceramic filter at different magnifications.

Pt, pure WO_3, and TiO_2 (P25) photocatalyst powder samples under visible light irradiation, as presented in Fig. 7. It could be clearly observed that there was nearly no decomposition with TiO_2 and very slow decomposition was observed on pure WO_3, whereas WO_3/Pt decomposed almost all the toluene after 90–180 min of LED-light exposure. Although there was some delay in the reaction rate of toluene decomposition in the 2nd and 3rd runs, almost complete photodecomposition was achieved after 90 min (1st run), 120 min (2nd run), and 180 min (3rd run) of light exposure, as seen from the graph reported in Fig. 7b. After 180 min of reaction time, the decomposition rates for WO_3/Pt, pure WO_3, and TiO_2 were calculated to be about 99%, 54%, and 12%, respectively. Therefore, WO_3/Pt could effectively decompose the gaseous toluene under indoor lighting condition. Since TiO_2 did not show any photodecomposition activity while pure WO_3 was a very poor photocatalyst, only WO_3/Pt was chosen for the further experiments, with the WO_3/Pt-coated ceramic filter (CFF) used as the support photocatalyst. Fig. 8 shows the photocatalytic decomposition of toluene performed with the blank and WO_3/Pt-coated CFF. From the plot of C/C_0 with the LED-light irradiation (Fig. 8a), it could be observed that the coated CFF

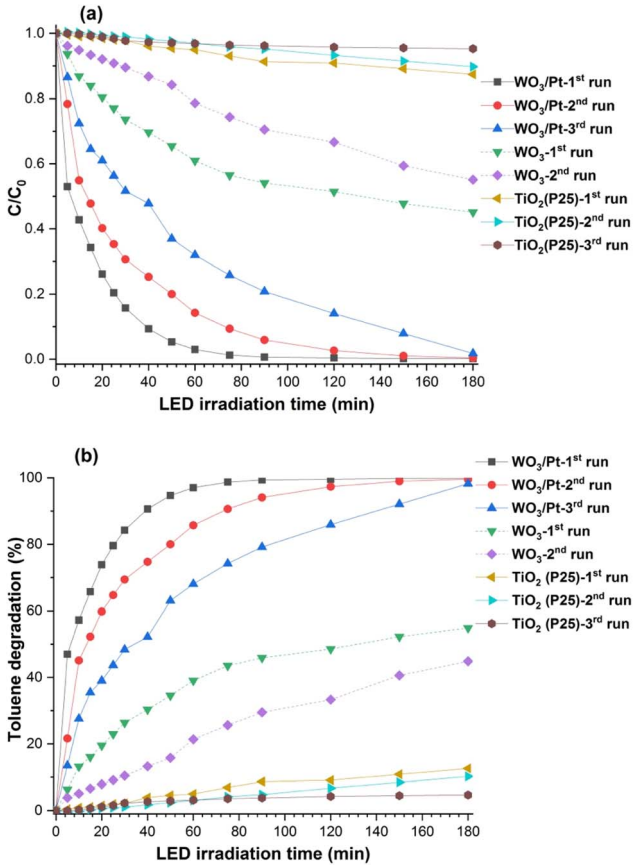

Fig. 7 (a) Plots of C/C_0 *vs.* visible light (LED) irradiation time inside the photoreactor with WO_3/Pt, pure WO_3, and TiO_2; C_0 represents the concentration of toluene (in ppm) before switching ON the LED light, and C is the toluene concentration with respect to the LED light exposure duration (in min), and (b) plots of toluene degradation (%) as a function of LED light exposure time.

could decompose almost all the toluene after 100 min of light exposure and the trend continued for even up to five consecutive runs, whereas the uncoated filter did not show any activity. The VOC-removal efficiency (% degradation of toluene) of the CFF was calculated according to the following equation

$$(\text{Efficiency})\% = (C_0 - C_t/C_0) \times 100 \quad (1)$$

where C_0 is the initial concentration of toluene (in ppm) just before switching on the LED light after attaining adsorption–desorption equilibrium and C_t is the concentration of toluene at different visible light exposure times (in minutes), as presented in Fig. 8b. From the graph, it can be seen that the degradation rate was almost saturated after 90 min of light exposure, indicating a complete decomposition of the gaseous toluene. The reaction rate slightly decreased after five consecutive cycles of the photodegradation test. A bar diagram of the results obtained from Fig. 8b is presented in Fig. 8c to easily visualize the percentage degradation in different cycles under different light exposure times. It is clearly evident that 35% of toluene was decomposed after 5 min of light exposure, and the value reached 100% after 110 min of reaction time. After the 5th run, the degradation rate decreased to 8% in the first 5 min, but became nearly as efficient as the 1st run after light exposure for 110 min, achieving a value of 92%. The decrease in the photodegradation rate at the initial stage of the reaction could be due to the adsorption of water molecules on the catalyst surface. It was noteworthy that five consecutive runs could be carried out inside the reactor without removing or pre-conditioning (annealing) the coated CFF prior to the next run. These data confirm the reusability and potential of the WO_3/Pt-coated CFF to be used as a filter medium in a photocatalytic air-filtration system for the elimination of VOCs.

The photocatalytic decomposition mechanism towards VOCs, including toluene, performed with different visible light-active catalysts as well as WO_3/Pt has been well reported.[42–45] As we used only WO_3/Pt nanoclusters as the coating material to deposit on the CFF surface without including any additives or surface modifiers, the reaction pathway for toluene decomposition would follow the similar mechanism that has been reported elsewhere (particularly those reporting at room temperature under visible light irradiation).[23,36,46,47]

The schematic illustration of toluene photodegradation performed with the WO_3/Pt-coated CFF is shown in Fig. 9. In this mechanism, upon visible light irradiation on the catalyst surface, e^-–h^+ pairs are generated by the excitation of the valence band electrons to the conduction band. PtNPs act as electron sinks, which actively prevent electron–hole recombination, thus allowing creating reactive oxygen species, such as superoxide ($O_2^{\bullet -}$) and hydroperoxyl ($HO_2^{\bullet}$) radicals and eventually hydrogen peroxide (H_2O_2), through multielectron reduction processes with the adsorbed O_2 molecules.[11,42,44,48,49] Meanwhile, the photogenerated holes can produce hydroxyl ($OH^{\bullet}$) radicals from the adsorbed water molecules on the catalyst surface. These reactive species, having a strong oxidizing power, can readily take part in the photo-oxidation process and interact with the gaseous toluene to break it down through either methyl group oxidation or aromatic ring opening and oxidation.[42,43]

According to the literature, the toluene oxidation process follows mainly two pathways: (i) initial oxidation stage to form benzaldehyde, which is then oxidized to benzoic acid followed by mineralization, with the end products CO_2 and H_2O, and (ii) intermediate benzyl radical formation, which are oxidized to benzyl alcohol or benzaldehyde and then further oxidized to benzoic acid, followed by the mineralization process.[42,43,45] In our case, as we used a TVOC (total VOC) sensing instrument, we could monitor any intermediate oxidized species formation during the photocatalysis process, thus increasing the toluene concentration at any intermediate point within the time course of the photodegradation. Since we tested the system in five consecutive runs, which followed a similar trend for the

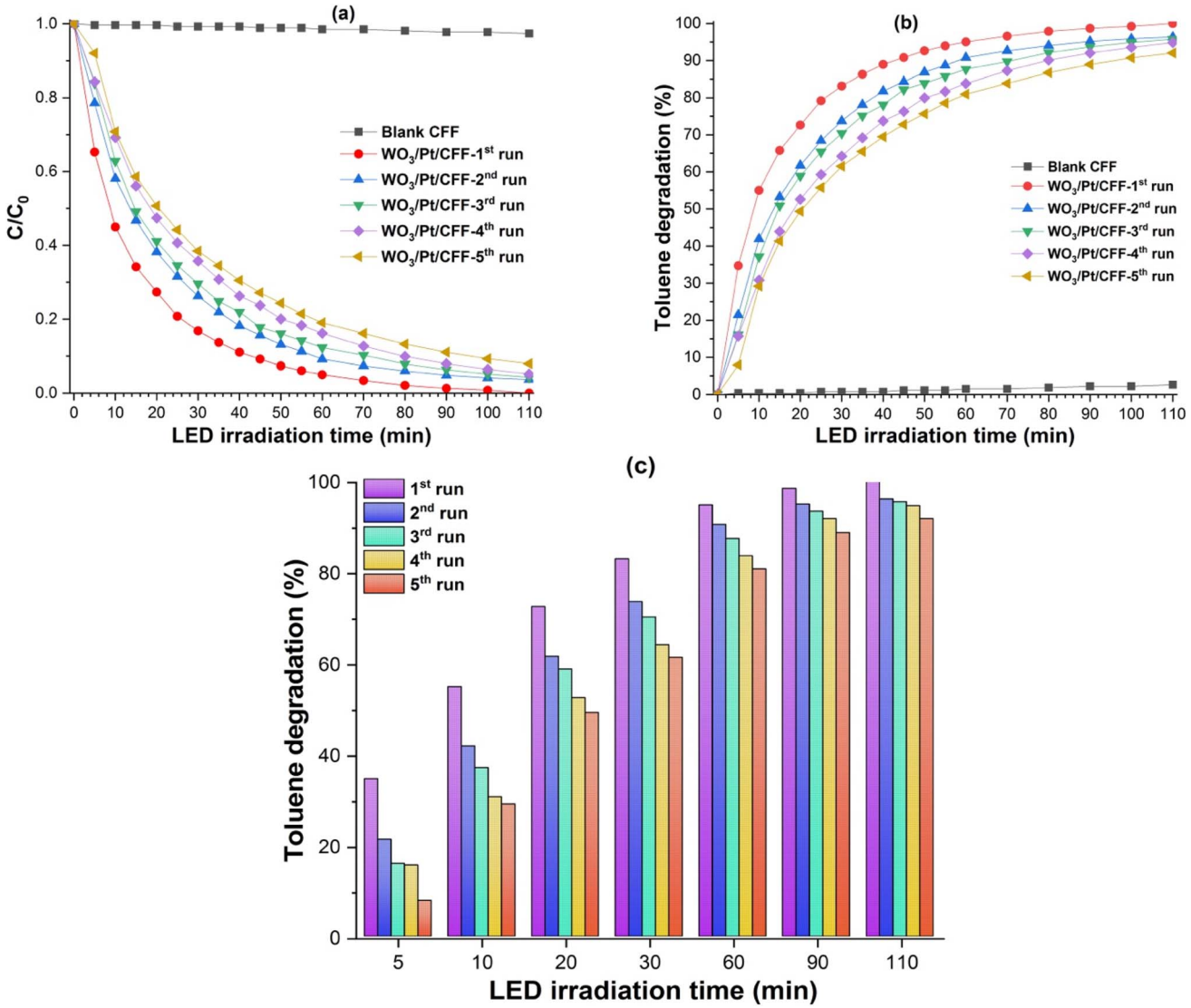

Fig. 8 (a) Plots of C/C_0 *vs.* visible light (LED) irradiation time inside the photoreactor with the blank and WO_3/Pt-coated CFF with five consecutive runs; C_0 represents the concentration of toluene (in ppm) before switching ON the LED light, and C is the toluene concentration with respect to the LED light exposure duration (in min), (b) plots of toluene degradation (%) as a function of LED light exposure time, and (c) comparison of the toluene degradation efficiencies at different cycles of the test.

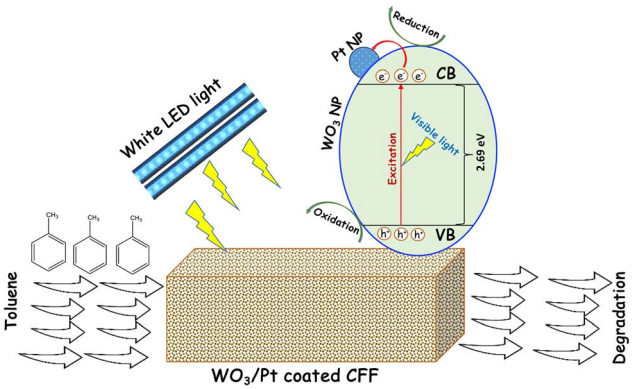

Fig. 9 Schematic of the proposed toluene photodegradation mechanism by the WO_3/Pt-coated CFF under visible light irradiation.

degradation curves, except for losing some efficiency, we can assume that the photodegradation may take place according to the first pathway. Nevertheless, the minimal losses in efficiency after multiple cycles, which is termed photocatalyst deactivation, could be attributed to the accumulation of some carbonaceous residues as well as moisture adsorption resulting from the photocatalytic process, as also observed by Weon *et al.*[50] This deficiency could be recovered by thermal treatment of the CFF whenever needed, as we have already observed (data not shown) and will present in our future work. Table 2 shows a comparative analysis of the photocatalytic decomposition of toluene performed with different visible light-active catalysts, including the WO_3/Pt nanocomposites in the present work. It can be seen that our supported catalyst filter looks very promising for the photocatalytic decomposition of toluene, particularly in the indoor environment.

Table 2 Comparison of the photocatalytic decomposition of toluene with different catalysts under visible light irradiation performed at room temperature

Photocatalyst	Toluene dose	Light source	Reactor	Decomposition efficiency/time	Ref.
Pt/WO_3 30 mg coated on a fibreglass membrane	200 ppm	300 Xe solar lamp	Stainless steel reactor with quartz window	97%, 30 min	51
Pt/WO_{3-x} coated on a 2 × 2 cm glass slide	20 ppm	460 nm emitting LED lamp	350 mL Pyrex glass reactor with quartz window	55% ($K = 0.0192$ min^{-1}), 40 min	44
Pd/WO_3 60 cm^2 coated film on a glass plate	0.03 μmol	Xe lamp (1 sun) $\lambda \geq 400$ nm	300 mL stainless steel cell with Pyrex window	~100%, 180 min	52
Pt–WO_3/TiO_2 50 mg	17.2 μmol	Blue LED ($\lambda \geq 420$ nm)	50 mL quartz cell	23.3%, 24 h	53
WO_3/Bi_2WO_6 200 mg spread on filter paper	—	300 Xe solar lamp with UV filter (>420 nm)	Quartz reactor	92%, 60 min	54
(001) facet TiO_2 nanotubes (30 × 273, 0.5 mm^3)	10 ppmv	150 W halogen lamp ($\lambda \geq 420$ nm)	300 mL glass reactor with quartz window	32.7%, 30 min	55
CuO/Bi_2MoO_6 100 mg	500 ppm	300 W Xe lamp 420 < λ < 750 nm	3.5 cm diameter quartz reactor	~99%, 120 min	56
Pt/TiO_{2-x} 0.02 g on a 2 × 4 cm quartz plate	100 ppm	300 W xenon lamp with 420 nm cut-off filter	150 mL Pyrex glass reactor with quartz window	~100%, 15 min	57
Au–WO_3/TiO_2 2 × 1 cm film	160 ppmv	365 nm LED lamp	15 mL quartz cell	95.4%, 30 min	29
Au–ZnAl/LDH 2 g	43.6–218 mg m^{-3}	500 W xenon lamp	Quartz reactor (500 × 100 × 25 mm)	66.4–98.9%, 180 min	58
Ag–TiO_2/PU	100 ppm	2 × 20 W (400–700 nm, 0.05 W cm^{-2})	2 × 4 × 15 cm^3 quartz reactor	85.2%, 360 min	59
Bi–TiO_2 deposited on a 50 mm diameter quartz plate	0.5 μL	300 Xe solar lamp	Home-made reactor	97%, 60 min	60
Cu–TiO_2/ACF 0.5 g	10 ppm	Fluorescent lamp	Photocatalytic reactor	47.8%, 60 min	61
g-C_3N_4/$NiWO_4$ 0.5 g	50 ppm	100 W visible light lamp	1 L batch quartz reactor	88.1%, 180 min	62
WO_3 (nanocube/nanosheets/nanorods) 20 mg	2–10 mmol	LED lamp ($\lambda \geq 400$ nm)	15 mL Schlenk tube	67–99%[a], 2–48 h	45
Nanodiamond/WO_3 coated on a 2 × 4 cm glass plate	20 ppmv	150 W halogen lamp with cut-off filter (λ > 420 nm)	300 mL Pyrex glass reactor with quartz window	~35%, 210 min	30
WO_3/Pt (~3 g) coated ceramic filter	50–60 ppm	White LED strip 48 W ($\lambda \geq 420$ nm)	3 L cylindrical quartz reactor	92–100%, 110 min	This work

[a] Oxidation of toluene to benzaldehyde.

4 Conclusion

Nanostructured platinum-doped tungsten oxide (WO_3/Pt) showed excellent visible light photoactivity to decompose organic dyes and gaseous toluene. Thanks to its narrow energy bandgap (2.7 eV), it can work under visible light irradiation and hence is suitable for use in indoor lighting conditions. The WO_3/Pt-coated ceramic filter was demonstrated to be highly efficient for the removal of toluene, which opens a possibility to use it for indoor air purification. In less than 2 h visible light irradiation, WO_3/Pt-CFF succeeded in eliminating nearly 99.9% of the initial toluene concentration. A similar trend in toluene decomposition was found even after five consecutive runs on the same photocatalyst, which shows the good reusability of the material, without much loss in the degradation efficiency. The porous nature of the ceramic filter favoured the uniform deposition of WO_3/Pt nanoparticles on its surface while its interconnected and open 3D assembly maximized the light diffusion and reflection capacity, which in fact increased the effective active sites of WO_3/Pt, further favouring the photocatalytic process. Since toluene belongs to the aromatic hydrocarbon group of VOCs (known as BTEX: benzene, toluene, ethylbenzene, and xylenes), our photocatalytic technique could be effective to remove other VOCs without re-contaminating the indoor airspace, which we would like to present in our future work. Our results also open the possibility of using porous ceramic-based substrates as the basis for air-purification devices in real environments. Our findings highlight the feasibility of using visible light to remediate air and water pollutants, paving a pathway for the development of new advanced purification technology.

Data availability

Experimental data supporting the findings of this work could be provided upon reasonable request.

Author contributions

Sudipto Pal: conceptualization, writing – original draft – review & editing, investigation, supervision, validation. Amruth

Kaitheri: resources, writing – original draft, data curation, formal analysis, methodology. Sanosh Kunjalukkal Padmanabhan: visualization, resources, supervision. Massimo Catalano: data curation, formal analysis, methodology. Stefano Perboni: conceptualization, funding acquisition, project administration, validation. Antonio Licciulli: conceptualization, supervision, validation.

Conflicts of interest

The authors declare no conflict of interest.

Acknowledgements

The authors thankfully acknowledge Mr Donato Canoletta for the XRD measurements and Dr Fabio Marzo for providing the SEM analyses. Nanohub srl is thankfully acknowledged for the financial support. Amruth Kaitheri acknowledges the financial support from PON scholarship funded by the Ministry of University and Research (MUR).

References

1 C. He, J. Cheng, X. Zhang, M. Douthwaite, S. Pattisson and Z. Hao, Recent Advances in the Catalytic Oxidation of Volatile Organic Compounds: A Review Based on Pollutant Sorts and Sources, *Chem. Rev.*, 2019, **119**, 4471–4568.

2 M. Maroni, B. Seifert and T. Lindvall, *Indoor Air Quality: A Comprehensive Reference Book*, Elsevier, 1995.

3 K. W. Shah and W. Li, A Review on Catalytic Nanomaterials for Volatile Organic Compounds VOC Removal and Their Applications for Healthy Buildings, *Nanomaterials*, 2019, **9**, 910.

4 O. US EPA, *What are volatile organic compounds (VOCs)?*, **https://www.epa.gov/indoor-air-quality-iaq/what-are-volatile-organic-compounds-vocs**, accessed 26 September 2024.

5 M. Ousmane, L. F. Liotta, G. D. Carlo, G. Pantaleo, A. M. Venezia, G. Deganello, L. Retailleau, A. Boreave and A. Giroir-Fendler, Supported Au catalysts for low-temperature abatement of propene and toluene, as model VOCs: support effect, *Appl. Catal., B*, 2011, **101**, 629–637.

6 D. B. Collins and D. K. Farmer, Unintended Consequences of Air Cleaning Chemistry, *Environ. Sci. Technol.*, 2021, **55**, 12172–12179.

7 W. Zhang, H. Cheng, Q. Niu, M. Fu, H. Huang and D. Ye, Microbial Targeted Degradation Pretreatment: A Novel Approach to Preparation of Activated Carbon with Specific Hierarchical Porous Structures, High Surface Areas, and Satisfactory Toluene Adsorption Performance, *Environ. Sci. Technol.*, 2019, **53**, 7632–7640.

8 G. T. Carroll and D. L. Kirschman, A Peripherally Located Air Recirculation Device Containing an Activated Carbon Filter Reduces VOC Levels in a Simulated Operating Room, *ACS Omega*, 2022, **7**, 46640–46645.

9 G. Zhang, A. Peyravi, Z. Hashisho, Z. Sun, Y. Liu, S. Zheng and L. Zhong, Integrated adsorption and photocatalytic degradation of VOCs using a TiO2/diatomite composite: effects of relative humidity and reaction atmosphere, *Catal. Sci. Technol.*, 2020, **10**, 2378–2388.

10 H. J. Kwon, D. S. Yang, M. S. Koo, S. M. Ji, J. Jeong, S. Oh, S. K. Kuk, H. Heo, D. J. Ham, M. Kim, H. Choi, J.-M. Lee, J.-W. Shur, W.-J. Lee, C.-O. Bin, N. Timofeev, H. Wu, L. Wang, T. Lee, D. J. Jacob and H. C. Lee, Long-lifetime water-washable ceramic catalyst filter for air purification, *Nat. Commun.*, 2023, **14**, 520.

11 Y. Zhang, Y. Wang, R. Xie, H. Huang, M. K. H. Leung, J. Li and D. Y. C. Leung, Photocatalytic Oxidation for Volatile Organic Compounds Elimination: From Fundamental Research to Practical Applications, *Environ. Sci. Technol.*, 2022, **56**, 16582–16601.

12 S. Pal, A. M. Laera, A. Licciulli, M. Catalano and A. Taurino, Biphase TiO2 Microspheres with Enhanced Photocatalytic Activity, *Ind. Eng. Chem. Res.*, 2014, **53**, 7931–7938.

13 A. Liciulli, R. Nisi, S. Pal, A. M. Laera, P. Creti and A. Chiechi, Photo-oxidation of ethylene over mesoporous Tio2/Sio2 catalysts, *Adv. Hortic. Sci.*, 2016, **30**, 75–80.

14 A. Anus, V. C. T. Le, M. Sheraz, S. Kim and W. R. Lee, Visible light-activated photocatalytic activity of TiO2–crystal violet based superhydrophobic paint against VOCs in indoor air, *Environ. Sci.: Adv.*, 2023, **2**, 69–77.

15 J. Song, X. Ren, G. Hu, L. Wang and X. Hu, Enhanced photocatalytic degradation of indoor formaldehyde by sepiolite decorated with TiO2 nanoparticles: effects of key preparation parameters, *Microporous Mesoporous Mater.*, 2023, **353**, 112515.

16 V. P. Barber, M. B. Goss, L. J. F. Deloya, L. N. LeMar, Y. Li, E. Helstrom, M. Canagaratna, F. N. Keutsch and J. H. Kroll, Indoor Air Quality Implications of Germicidal 222 nm Light, *Environ. Sci. Technol.*, 2023, **57**(42), 15990–15998.

17 F. Graeffe, Y. Luo, Y. Guo and M. Ehn, Unwanted Indoor Air Quality Effects from Using Ultraviolet C Lamps for Disinfection, *Environ. Sci. Technol. Lett.*, 2023, **10**, 172–178.

18 M. F. Link, A. Shore, B. H. Hamadani and D. Poppendieck, Ozone Generation from a Germicidal Ultraviolet Lamp with Peak Emission at 222 nm, *Environ. Sci. Technol. Lett.*, 2023, **10**, 675–679.

19 S. Weon, F. He and W. Choi, Status and challenges in photocatalytic nanotechnology for cleaning air polluted with volatile organic compounds: visible light utilization and catalyst deactivation, *Environ. Sci.: Nano*, 2019, **6**, 3185–3214.

20 F. He, W. Jeon and W. Choi, Photocatalytic air purification mimicking the self-cleaning process of the atmosphere, *Nat. Commun.*, 2021, **12**, 2528.

21 J. Kim, C. W. Lee and W. Choi, Platinized WO_3 as an Environmental Photocatalyst that Generates OH Radicals under Visible Light, *Environ. Sci. Technol.*, 2010, **44**(17), 6849–6854.

22 T. T. Nguyen, S.-N. Nam, J. Son and J. Oh, Tungsten Trioxide (WO3)-assisted Photocatalytic Degradation of Amoxicillin by Simulated Solar Irradiation, *Sci. Rep.*, 2019, **9**, 9349.

23 J. Kim, H. Lee, M. Kim, Y.-Y. Ahn, Y.-J. Ko, H.-S. Oh, M. Kang, M. W. Chung, S. Weon, M. Cho, H. Lee and J. Lee, Room-

Temperature Preparation of Platinized Nonstoichiometric Tungsten Oxide via Platinum Photodeposition Followed by Chemical Reduction: Kinetic Enhancement of Photocatalytic Oxidation and Disinfection under Low-Intensity Visible-Light Irradiation, *ACS ES&T Eng.*, 2023, **3**, 1770–1786.

24 J. A. Herron, J. Kim, A. A. Upadhye, G. W. Huber and C. T. Maravelias, A general framework for the assessment of solar fuel technologies, *Energy Environ. Sci.*, 2015, **8**, 126–157.

25 M. Miyauchi, Photocatalysis and photoinduced hydrophilicity of WO3 thin films with underlying Pt nanoparticles, *Phys. Chem. Chem. Phys.*, 2008, **10**, 6258–6265.

26 R. Abe, H. Takami, N. Murakami and B. Ohtani, Pristine Simple Oxides as Visible Light Driven Photocatalysts: Highly Efficient Decomposition of Organic Compounds over Platinum-Loaded Tungsten Oxide, *J. Am. Chem. Soc.*, 2008, **130**(25), 7780–7781.

27 S. Weon, F. He and W. Choi, Status and challenges in photocatalytic nanotechnology for cleaning air polluted with volatile organic compounds: visible light utilization and catalyst deactivation, *Environ. Sci.: Nano*, 2019, **6**, 3185–3214.

28 P. Dong, G. Hou, X. Xi, R. Shao and F. Dong, WO3-based photocatalysts: morphology control, activity enhancement and multifunctional applications, *Environ. Sci.: Nano*, 2017, **4**, 539–557.

29 X. Wang, H. Pan, M. Sun and Y. Zhang, Au single atom-anchored WO3/TiO2 nanotubes for the photocatalytic degradation of volatile organic compounds, *J. Mater. Chem. A*, 2022, **10**, 6078–6085.

30 H. Kim, H. Kim, S. Weon, G. Moon, J.-H. Kim and W. Choi, Robust Co-catalytic Performance of Nanodiamonds Loaded on WO3 for the Decomposition of Volatile Organic Compounds under Visible Light, *ACS Catal.*, 2016, **6**, 8350–8360.

31 G. Huang, L. Liu, L. Chen, L. Gao, J. Zhu and H. Fu, Unique insights into photocatalytic VOCs oxidation over WO3/carbon dots nanohybrids assisted by water activation and electron transfer at interfaces, *J. Hazard. Mater.*, 2022, **423**, 127134.

32 J. Kim, J. Park, M. S. Koo, W. S. Cho, S. Moon, I. Hwang, J. Kim, J. Y. Park, D. J. Ham, H. C. Lee and J. K. Kim, High-Performance Ceramic Catalyst Filters with Textured Waveguides for Efficient Removal of Volatile Organic Compounds, *Adv. Opt. Mater.*, 2024, **12**, 2400746.

33 T. Wei, X. Chen and Z. Guo, Ceramic membrane composites for highly efficient oil–water separation: a review, *J. Mater. Chem. A*, 2024, **12**, 20803–20837.

34 L. Lang, H. Zhu, Y. Ding, X. Yin, C. Wu, X. Yu and A. V. Bridgwater, Mini-Review on Hot Gas Filtration in Biomass Gasification: Focusing on Ceramic Filter Candles, *Energy Fuels*, 2021, **35**, 11800–11819.

35 Y. Zhao, Z.-X. Low, S. Feng, Z. Zhong, Y. Wang and Z. Yao, Multifunctional hybrid porous filters with hierarchical structures for simultaneous removal of indoor VOCs, dusts and microorganisms, *Nanoscale*, 2017, **9**, 5433–5444.

36 Z. Wen, W. Wu, Z. Liu, H. Zhang, J. Li and J. Chen, Ultrahigh-efficiency photocatalysts based on mesoporous Pt–WO3 nanohybrids, *Phys. Chem. Chem. Phys.*, 2013, **15**, 6773–6778.

37 D. Hidayat, A. Purwanto, W.-N. Wang and K. Okuyama, Preparation of size-controlled tungsten oxide nanoparticles and evaluation of their adsorption performance, *Mater. Res. Bull.*, 2010, **45**, 165–173.

38 M. Thommes, K. Kaneko, A. V. Neimark, J. P. Olivier, F. Rodriguez-Reinoso, J. Rouquerol and K. S. W. Sing, Physisorption of gases, with special reference to the evaluation of surface area and pore size distribution (IUPAC Technical Report), *Pure Appl. Chem.*, 2015, **87**, 1051–1069.

39 S. Pal and G. De, Formation of Au–Pt bimetallic nanoparticles in a two-layer SiO2 films doped with Au and Pt, respectively, through interlayer diffusion, *Phys. Chem. Chem. Phys.*, 2008, **10**, 4062–4066.

40 Z. Huang, Y. Miseki and K. Sayama, Solar-light-driven photocatalytic production of peroxydisulfate over noble-metal loaded WO3, *Chem. Commun.*, 2019, **55**, 3813–3816.

41 S. S. Kalanur, Y. J. Hwang, S. Y. Chae and O. S. Joo, Facile growth of aligned WO3 nanorods on FTO substrate for enhanced photoanodic water oxidation activity, *J. Mater. Chem. A*, 2013, **1**, 3479–3488.

42 Y. Tulebekov, Z. Orazov, B. Satybaldiyev, D. D. Snow, R. Schneider and B. Uralbekov, Reaction Steps in Heterogeneous Photocatalytic Oxidation of Toluene in Gas Phase—A Review, *Molecules*, 2023, **28**, 6451.

43 C. Liang, C. Li, Y. Zhu, X. Du, C. Yao, Y. Ma and J. Zhao, Recent advances of photocatalytic degradation for BTEX: materials, operation, and mechanism, *Chem. Eng. J.*, 2023, **455**, 140461.

44 J. Kim, H. Lee, M. Kim, Y.-Y. Ahn, Y.-J. Ko, H.-S. Oh, M. Kang, M. W. Chung, S. Weon, M. Cho, H. Lee and J. Lee, Room-Temperature Preparation of Platinized Nonstoichiometric Tungsten Oxide via Platinum Photodeposition Followed by Chemical Reduction: Kinetic Enhancement of Photocatalytic Oxidation and Disinfection under Low-Intensity Visible-Light Irradiation, *ACS ES&T Eng.*, 2023, **3**, 1770–1786.

45 A. Singha, J. Kaishyop, T. S. Khan and B. Chowdhury, Visible-Light-Driven Toluene Oxidation to Benzaldehyde over WO3 Nanostructures, *ACS Appl. Nano Mater.*, 2023, **6**, 21818–21828.

46 S. K. Sharma, T. S. Khan, A. Sarkar, U. Das, T. Tyagi, S. Vadivel, S. Das, A. Puzari and B. Paul, Pt Nanoparticles Supported on WO3 Microparticles as the Catalyst for the Oxidation of Toluene, *ACS Appl. Nano Mater.*, 2024, **7**, 4014–4023.

47 X. Wang, J. Deng, Y. Liu, L. Jing, L. Wu, Y. Feng, X. Zhou, Z. Hao and H. Dai, Mesoporous Si-WO3-supported Pt catalysts with high catalytic performance and excellent water resistance for toluene oxidation, *Catal. Today*, 2024, **432**, 114650.

48 J.-J. Li, M. Zhang, B. Weng, X. Chen, J. Chen and H.-P. Jia, Oxygen vacancies mediated charge separation and collection in Pt/WO3 nanosheets for enhanced

photocatalytic performance, *Appl. Surf. Sci.*, 2020, **507**, 145133.

49 Z. Chen, Y. Peng, J. Chen, C. Wang, H. Yin, H. Wang, C. You and J. Li, Performance and Mechanism of Photocatalytic Toluene Degradation and Catalyst Regeneration by Thermal/UV Treatment, *Environ. Sci. Technol.*, 2020, **54**, 14465–14473.

50 S. Weon and W. Choi, TiO2 Nanotubes with Open Channels as Deactivation-Resistant Photocatalyst for the Degradation of Volatile Organic Compounds, *Environ. Sci. Technol.*, 2016, **50**, 2556–2563.

51 J.-J. Li, M. Zhang, B. Weng, X. Chen, J. Chen and H.-P. Jia, Oxygen vacancies mediated charge separation and collection in Pt/WO3 nanosheets for enhanced photocatalytic performance, *Appl. Surf. Sci.*, 2020, **507**, 145133.

52 T. Arai, M. Horiguchi, M. Yanagida, T. Gunji, H. Sugihara and K. Sayama, Complete oxidation of acetaldehyde and toluene over a Pd/WO3 photocatalyst under fluorescent- or visible-light irradiation, *Chem. Commun.*, 2008, 5565–5567.

53 S. Higashimoto, K. Katsuura, M. Yamamoto and M. Takahashi, Photocatalytic activity for decomposition of volatile organic compound on Pt-WO3 enhanced by simple physical mixing with TiO2, *Catal. Commun.*, 2020, **133**, 105831.

54 Y. Jia, X. Zhang, R. Wang, J. Yuan, R. Zheng, J. Zhang, F. Qian, Y. Chen, M. Zhang and L. Guo, Energy band engineering of WO3/Bi2WO6 direct Z-scheme for enhanced photocatalytic toluene degradation, *Appl. Surf. Sci.*, 2023, **618**, 156636.

55 S. Weon, E. Choi, H. Kim, J. Y. Kim, H.-J. Park, S. Kim, W. Kim and W. Choi, Active {001} Facet Exposed TiO2 Nanotubes Photocatalyst Filter for Volatile Organic Compounds Removal: From Material Development to Commercial Indoor Air Cleaner Application, *Environ. Sci. Technol.*, 2018, **52**, 9330–9340.

56 H. Wang, Y. Wang, C. Jiang, K. Ye, X. He, C. Xue, Z. Yang, X. Zhou and H. Ji, Hybridization of CuO with Bi2MoO6 Nanosheets as a Surface Multifunctional Photocatalyst for Toluene Oxidation under Solar Irradiation, *ACS Appl. Mater. Interfaces*, 2020, **12**, 2259–2268.

57 H. Mao, M. Xu, S. Li, Y. Ren, Y. Zhao, J. Yu, Q. Zhang, W. Zhao, G. Zhang, L. Yan, Z. Xu and Z. Bian, Accelerating Surface Lattice Oxygen Activation of Pt/TiO2–x by Modulating the Interface Electron Interaction for Efficient Photocatalytic Toluene Oxidation, *ACS ES&T Eng.*, 2023, **3**, 1851–1863.

58 X. Zhang, L. Wang, X. Zhou, Z. Ni and S. Xia, Investigation into the Enhancement of Property and the Difference of Mechanism on Visible Light Degradation of Gaseous Toluene Catalyzed by ZnAl Layered Double Hydroxides before and after Au Support, *ACS Sustain. Chem. Eng.*, 2018, **6**, 13395–13407.

59 T.-D. Pham, B.-K. Lee and D. Pham-Cong, Advanced removal of toluene in aerosol by adsorption and photocatalytic degradation of silver-doped TiO2/PU under visible light irradiation, *RSC Adv.*, 2016, **6**, 25346–25358.

60 M. Lai, J. Zhao, Q. Chen, S. Feng, Y. Bai, Y. Li and C. Wang, Photocatalytic toluene degradation over Bi-decorated TiO2: promoted O2 supply to catalyst's surface by metallic Bi, *Catal. Today*, 2019, **335**, 372–380.

61 J. Kim and B.-K. Lee, Enhanced photocatalytic decomposition of VOCs by visible-driven photocatalyst combined Cu-TiO2 and activated carbon fiber, *Process Saf. Environ. Prot.*, 2018, **119**, 164–171.

62 V.-D. Dao, L. T. Son, T. D. Nguyen, N. Van Noi, N. M. Ngoc, T.-D. Pham, P. Van Quan and H. T. Trang, Superior visible light photocatalytic activity of g-C3N4/NiWO4 direct Z system for degradation of gaseous toluene, *J. Solid State Chem.*, 2019, **272**, 62–68.